Robotica: (2019) volume 37, pp. 1513–1532. © Cambridge University Press 2019
doi:10.1017/S0263574719000092

Unified Kinematics of Prismatically Actuated Parallel Delta Robots

Eray A. Baran†*, Ozhan Ozen‡, Dogacan Bilgili§ and Asif Sabanovic§

†*Mechatronics Engineering, Istanbul Bilgi University, Istanbul, Turkey*
‡*Gerontechnology & Rehabilitation, ARTORG Center for Biomedical Engineering Research, University of Bern, Bern, Switzerland*
§*Mechatronics Engineering, Sabanci University, Istanbul, Turkey*

(Accepted 9 January 2019. First published online: February 15, 2019)

SUMMARY
This paper presents a unified formulation for the kinematics, singularity and workspace analyses of parallel delta robots with prismatic actuation. Unlike the existing studies, the derivations presented in this paper are made by assuming variable angles and variable link lengths. Thus, the presented scheme can be used for all of the possible linear delta robot configurations including the ones with asymmetric kinematic chains. Referring to a geometry-based derivation, the paper first formulates the position and the velocity kinematics of linear delta robots with non-iterative exact solutions. Then, all of the singular configurations are identified assuming a parametric content for the Jacobian matrix derived in the velocity kinematics section. Furthermore, a benchmark study is carried out to determine the linear delta robot configuration with the maximum cubic workspace among symmetric and semi-symmetric kinematic chains. In order to show the validity of the proposed approach, two sets of experiments are made, respectively, on the horizontal and the Keops type of linear delta robots. The experiment results for the confirmation of the presented kinematic analysis and the simulation results for the determination of the maximum cubic workspace illustrate the efficacy and the flexible applicability of the proposed framework.

KEYWORDS: Linear Delta Robot; Unified Kinematics; Asymmetric Delta Robot; Maximum Symmetric Workspace; Generalized Singularities.

Nomenclature

Ψ_*	Reference frame $*$
$R_{*,\dagger}$	Rotation matrix around axis $*$ by angle $\dagger$
T_*	Translation vector $*$
α_*	Angle between base plane and joint axis $*$
d_*	Distance traveled by actuator $*$
r_e	Radius of the circumcircle of the end effector triangle
r_b	Radius of the circumcircle of the base triangle
l_*	Length of link between actuator $*$ and corresponding edge of end effector triangle
θ_*	Angle between x-axis of base triangle and projection of link $*$

1. Introduction

Recent progress in robotics paved the way toward development of manipulators with various kinematic chains that can meet the application requirements.[1] Today, numerous types of robots are used in applications such as pick and place operations,[2] assembly duties,[3] haptic rendering[4] or

* Corresponding author. E-mail: eray.baran@bilgi.edu.tr

https://doi.org/10.1017/S0263574719000092 Published online by Cambridge University Press

high-precision positioning.[5] Among these manipulators, structures with parallel kinematic configurations have caught much attention due to their superiority in providing faster response. Unlike serial structures, in parallel manipulators, the actuators are located at the stationary base and the load of the links is shared by each joint, resulting in lighter structures.[6] In addition to the loading advantage, parallel manipulators also provide a better alternative for high-precision tasks since the accumulation of positioning errors due to inertial disturbances is smaller in such configurations. The research in parallel robots has mainly focused on the problems of workspace optimization,[7,8] dimensional synthesis,[9] and analysis of kinematics and dynamics.[10,11]

The studies dealing with the optimization mostly focus on the acquisition of the configuration parameters in order to attain the maximum workspace volume.[12,13] In ref.,[14] for example, authors discuss the optimization of a parallel manipulator with two possible configurations, aiming to obtain the maximum workspace volume. In ref.[15] a constrained optimization procedure for a delta-4 type robot is given taking into consideration prespecified workspace boundaries. A more detailed study is given in,[16] where multicriteria optimization of a parallel rehabilitation robot is made considering aspects such as force response, workspace utilization, stiffness and condition number. Other studies concerned with multiobjective optimization of parallel machines take into consideration the optimality criteria such as workspace boundary, condition number, accuracy and stiffness.[17–20] Some interesting optimization results are shown in ref.[21] where the variation of motor axis inclinations is studied for a 3-DOF parallel manipulator. Optimization has also been used as a tool to have better kinematic design either compromising between manipulability and the utilized workspace of the system,[22] or providing singularity-free maximal workspace.[23]

Another focus point in the research of parallel robots is the analysis and synthesis of kinematic chains.[24] In many applications, the analysis of kinematic chain requires iterative approaches such as Newton–Raphson method, which is a computationally expensive practice.[25,26] In that sense, a major problem in the kinematics analysis is to formulate solution algorithms that do not contain nested vector loops, and hence simplify the kinematic computations. Among the existing studies, the most straightforward approach is to adopt a geometry-based derivation of kinematics equations with exact solutions.[27,28] This approach, however, might not always be feasible especially when the system under consideration has a complex geometric structure. For such systems, some researchers have proposed alternative methods like artificial neural network (ANN) and quaternion-based solution of kinematic chains as shown in refs.[29] and,[30] respectively. Further examples of studies dealing with the synthesis of large workspace parallel mechanisms, particularly to be used in machining, can be found in refs.[31] and.[32] Among 3-DOF parallel manipulators, the delta robot with prismatic actuation (i.e., the linear delta robot) has recently caught more attention because of its advantages like very rapid positioning with high accuracy and improved stiffness.[33,34] The linear delta structure can be particularly important for applications like ultra-fast 3D printing[35] or for haptic feedback generation once occupied with direct drive actuators.[36] Motivated from those advantages, this paper investigates a unified and fully parametric kinematics formulation for the linear delta robot family. In order to achieve this goal, first the derivation of the forward and the inverse kinematics algorithms are made, which is then followed by the formulation of the velocity kinematics and the kinematic Jacobian. Making use of the Jacobian matrix obtained in parametric form, the study is extended to find out all of the singular configurations of linear delta robots. Finally, benefitting from this unified formulation, a benchmark study is carried out to identify the maximum cubic workspace among the symmetric and semi-symmetric configurations. Even though all of the kinematics, singularity and workspace analyses of linear delta robots have well been studied by other researchers, to the best of authors' knowledge, yet there is no study that unifies these concepts in a fully parametric framework. The novelties introduced throughout this study can be listed as follows:

- Formulation of position- and velocity-level kinematics using a parametric, geometry-based analysis: The contribution brought with the presented derivation allows simplified computation of kinematics for linear delta robots that have different and potentially asymmetric configurations, as illustrated in Figs. 2–4. In the presented formulation, both the climbing angle (i.e., the angle between the base and the linear actuators) and the angles between the vertical projection planes of the actuators are kept parametric. Hence, the presented scheme can be utilized for all delta configurations including horizontal,[37] vertical[38] and Keops or pyramidal[39] type of linear delta robots and even for the ones with asymmetric kinematic chains. Moreover, novel mechanisms

https://doi.org/10.1017/S0263574719000092 Published online by Cambridge University Press

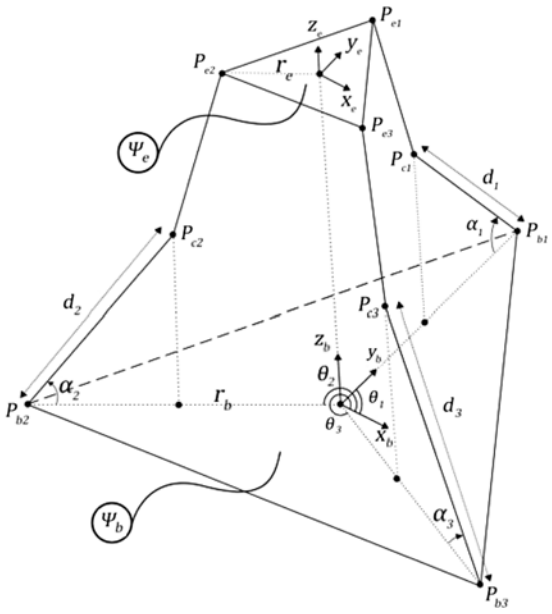
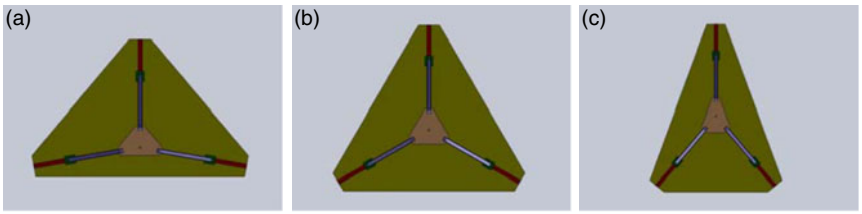


Fig. 1. Schematic representation of delta robot geometry.



Configuration with angles: $\theta_1 = 90^o, \theta_2 = 190^o$ $\theta_3 = 350^o$

Configuration with angles: $\theta_1 = 90^o, \theta_2 = 210^o$ $\theta_3 = 330^o$

Configuration with angles: $\theta_1 = 90^o, \theta_2 = 230^o$ $\theta_3 = 310^o$

Fig. 2. Variation of angle θ_i between the projections of prismatic actuator axes.

making use of delta structure with prismatic actuation[40] can also be analyzed with the proposed generalized framework.

- Following the same generalized approach, the kinematic Jacobian (**J**) is obtained again in the parametric form which is then investigated for the rank deficient configurations. The presented study identifies all of the possible singularities that can exist in a linear delta robot.
- Another benefit of the presented study is the possibility of making multiobjective and multicriteria optimization during design process of delta robots. Since the attack angle α_i, axial orientation θ_i and the link lengths l_i's are kept parametric (see Fig. 1), one can make analytical optimization and come up with novel designs satisfying certain predefined criteria. In order to address this feature, a benchmark study is carried out in this paper, where the maximum cubic workspace of symmetric and semi-symmetric linear delta configurations are obtained.
- Possibility to design ultra-high-precision positioning systems: The asymmetric design flexibility introduced with the parametric formulation provided in this study can open the doors for systems that have very high precision in certain axes. For instance, considering an extreme case of configuration as shown in Fig. 2(C), it is possible to obtain end effector motion with sub-encoder resolution in one axis if a very small value is taken for the angle between the joints 2 and 3.

The organization of the paper is given as follows. In Section 2, the generalized formulation of system geometry is presented. In Section 3, position-level forward kinematics is derived. Similarly, Section 4 presents the analysis of position-level inverse kinematics. Section 5 explains the velocity-level kinematics of the system which is followed by a parametric analysis for the singular configurations in Section 6. In Section 7, the experimental validation of the presented model is made

https://doi.org/10.1017/S0263574719000092 Published online by Cambridge University Press

using two variants of linear delta robots and a 3-DOF high-precision Cartesian robot. In Section 8, a benchmark study is carried out to determine the maximum cubic workspace of semi-symmetric configurations with an isosceles base triangle. Finally, in Section 9, conclusions are outlined along with the future work related to this study.

2. Formulation of System Geometry

In the following derivation, the mathematical formulation to obtain the forward and inverse kinematic solutions of linear delta robots is presented. Inspired by the derivations given in refs.[41] and,[42] the flexibility of applications for linear delta robots with asymmetric configuration is preserved in this investigation. The derivation refers to the geometry and variables (i.e., link lengths, points and angles) shown in Fig. 1. Let us assume that two coordinate frames, $\Psi_b = [x_b, y_b, z_b]^T$ and $\Psi_e = [x_e, y_e, z_e]^T$, are placed at the circumcenter of the base and the end effector triangles, respectively. It is implicitly assumed that the angles between the horizontal projections of any two links of the manipulator measured on the plane including points P_{b1}, P_{b2} and P_{b3} are always below π radians. Hence, the circumcenters of these triangles always sit inside the area covered by their edges. Using this representation, the position mapping between the two coordinate frames can be given as follows:

$$\Psi_e = \Psi_b + \Xi \tag{1}$$

where $\Xi = [x, y, z]^T$ is the variable of interest in forward kinematics problem (i.e., the end effector coordinates with respect to origin set in the manipulator base). Following this definition, the coordinates of the end effector triangle corners, P_{ei}, expressed with respect to the base frame can be given by

$$P_{ei} = \Psi_e + R_{z,\theta_i} T_e \tag{2}$$

where $R_{z,\theta_i} \in SO(3)$ and $T_e = [r_e, 0, 0]^T$ stand for the rotation matrix around z-axis by an angle of θ_i and translation vector along x-axis by a magnitude of r_e. In the most general case, variation of the angle θ_i would enable generation of asymmetric geometries for the manipulator. This will provide a design flexibility based on the desired precision requirements for certain axes of the end effector. For the derivation given in this paper, the range of angles θ_i are assumed to satisfy $\theta_1 \in [0, 2\pi]$, $\left(\theta_1 + \frac{\pi}{2}\right) < \theta_2 < (\theta_1 + \pi)$ and $\left(\theta_2 + \frac{\pi}{2}\right) < \theta_3 < (\theta_2 + \pi)$. Some examples of asymmetric configurations obtained by varying angle θ_i are shown in Fig. 2.

By substituting (1) into (2), one can obtain the following identity:

$$P_{ei} = \Psi_b + \Xi + R_{z,\theta_i} T_e \tag{3}$$

Similarly, the coordinates of the base triangle corners P_{bi} can be given as follows:

$$P_{bi} = \Psi_b + R_{z,\theta_i} T_b \tag{4}$$

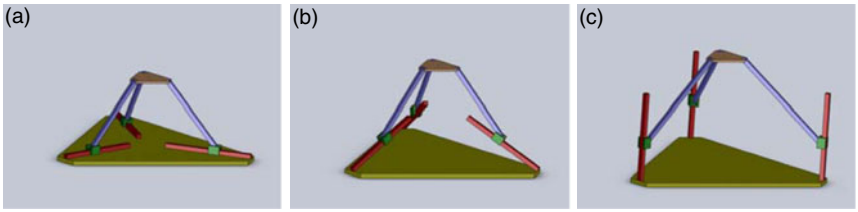
where $T_b = [r_b, 0, 0]^T$ represents the translation vector along x-axis by a magnitude of r_b. Assuming that each actuator i realizes a translation of magnitude d_i along its axis of motion, one can represent the coordinates of the tip of actuators, P_{ci}, expressed in the base frame as follows:

$$P_{ci} = \Psi_b + R_{z,\theta_i} T_b + R_{z,\theta_i} R_{y,\phi_i} T_{di} \tag{5}$$

where $T_{di} = [0, 0, d_i]^T$ and $\phi_i = \alpha_i - \pi/2$ stand for the translation vector along z-axis by a magnitude of d_i and for the counter-clockwise rotation angle of the ith actuator around its own y-axis, respectively. Keeping a parametric value for the attack angle α_i brings further design flexibility based on the desired application. Since different attack angles for different joints of the same robot can potentially be preferred for some applications, one can come up with a highly asymmetric configuration, which could still be modeled with the approach presented here. In the derivation given below, this angle is assumed to be bounded between 0° and 90° (i.e., $0 \leq \alpha_i \leq \frac{\pi}{2}$). Some examples of the symmetric and asymmetric configurations are illustrated in Figs. 3 and 4, respectively.

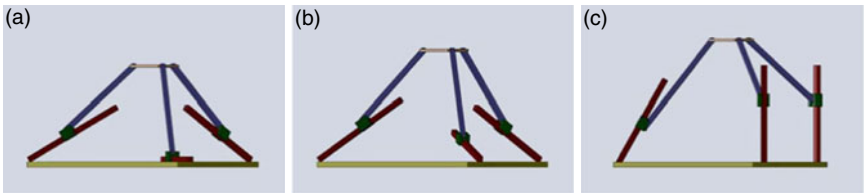
Since the definitions of the points representing the system's geometry are all made with respect to the base axis, one can now insert the final constraint and formulate the fundamental equations for forward and inverse kinematics of the system. Assuming that the links between the points P_{ci} and P_{ei} have the lengths l_i, the constraining equation of the system can be given as follows:

https://doi.org/10.1017/S0263574719000092 Published online by Cambridge University Press



Horizontal configuration $\alpha_1 = \alpha_2 = \alpha_3 = 0^o$ | Keops configuration $\alpha_1 = \alpha_2 = \alpha_3 = 30^o$ | Vertical configuration $\alpha_1 = \alpha_2 = \alpha_3 = 90^o$

Fig. 3. Variation of angle α_i between the prismatic actuators and the base frame for some symmetric configurations.



Asymmetry example 1 $\alpha_1 = 0^o, \alpha_2 = 30^o$ $\alpha_3 = 30^o$ | Asymmetry example 2 $\alpha_1 = 15^o, \alpha_2 = 30^o$ $\alpha_3 = 45^o$ | Asymmetry example 3 $\alpha_1 = 90^o, \alpha_2 = 90^o$ $\alpha_3 = 60^o$

Fig. 4. Variation of angle α_i between the prismatic actuators and the base frame for some asymmetric configurations.

$$\| P_{ei} - P_{ci} \| = l_i \tag{6}$$

where $\|.\|$ represents the L_2 norm of its argument. Substituting (2) and (5) into (6), one can obtain the following identity:

$$\| \Xi + R_{z,\theta_i} T_e - R_{z,\theta_i} T_b - R_{z,\theta_i} R_{y,\phi_i} T_{di} \| = l_i \tag{7}$$

Equation (7) can be recast by inserting the contents of the vectors Ξ, T_e, T_b, and the matrices R_{z,θ_i}, R_{y,ϕ_i} as follows:

$$\left\| \begin{bmatrix} x + (r_e - r_b + d_i c\alpha_i)\, c\theta_i \\ y + (r_e - r_b + d_i c\alpha_i)\, s\theta_i \\ z - d_i s\alpha_i \end{bmatrix} \right\| = l_i \tag{8}$$

where $c*$ and $s*$ stand for the abbreviations of the cosine and sine of the angle $*$. Expanding the norm in (8), one can finally obtain the following quadratic equation:

$$(x + c\theta_i\, (r_e - r_b + d_i c\alpha_i))^2 + (y + s\theta_i\, (r_e - r_b + d_i c\alpha_i))^2 + (z - d_i s\alpha_i)^2 = l_i^2 \tag{9}$$

The identity given in (9) for $i = 1, 2, 3$ contains three equations with three unknowns for each case of forward and inverse kinematics. In forward kinematics, the lengths d_i's are known and the unknowns of the equations are the end effector positions $[x, y, z]^T$. Similarly, in inverse kinematics, the lengths d_i's are unknowns to be calculated from the given end effector positions $[x, y, z]^T$.

3. Position-level Forward Kinematics

The solution to the forward kinematics problem is obtained from the intersection points of the surfaces of three spheres, with the corners of a triangle that is parallel to the base plane. As illustrated in Fig. 5, this intersection can as well be at a point which corresponds to the lower arm configuration of the delta robot. Hence, there exist two solutions for each of x, y and z variables.
Referring back to (9), one can rearrange the terms and come up with the following expression:

$$x^2 + y^2 + z^2 + \sigma_{1i} x + \sigma_{2i} y + \sigma_{3i} z - \lambda_i = 0 \tag{10}$$

https://doi.org/10.1017/S0263574719000092 Published online by Cambridge University Press

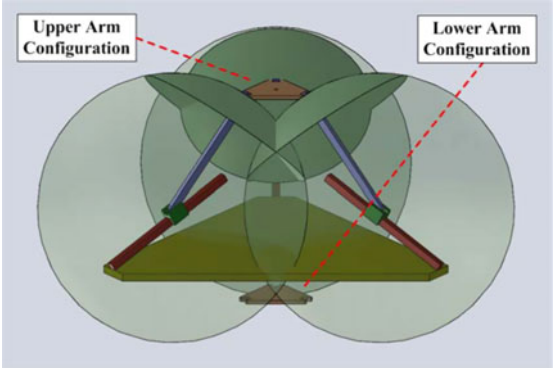


Fig. 5. Illustration of upper and lower arm configurations.

where the terms σ_{1i}, σ_{2i} σ_{3i} and λ_i have the following content:

$$\sigma_{1i} = 2c\theta_i\,(d_i c\alpha_i + r_e - r_b) \tag{11}$$

$$\sigma_{2i} = 2s\theta_i\,(d_i c\alpha_i + r_e - r_b) \tag{12}$$

$$\sigma_{3i} = -2d_i s\alpha_i \tag{13}$$

$$\lambda_i = l_i^2 - d_i^2 - (r_e - r_b)^2 - 2d_i r_e c\alpha_i + 2d_i r_b c\alpha_i \tag{14}$$

The expression given in (10) contains three linearly independent equations that include both first- and second-order terms which makes it difficult to solve. However, the quadratic terms in (10) can be eliminated by proper subtractions of the hidden equations for $i = 1, 2, 3$ from one another, which gives the following equation system:

$$(\sigma_{11} - \sigma_{13})\,x + (\sigma_{21} - \sigma_{23})\,y + (\sigma_{31} - \sigma_{33})\,z = (\lambda_1 - \lambda_3) \tag{15}$$

$$(\sigma_{12} - \sigma_{13})\,x + (\sigma_{22} - \sigma_{23})\,y + (\sigma_{32} - \sigma_{33})\,z = (\lambda_2 - \lambda_3) \tag{16}$$

Equations (15) and (16) can be recast as a linear matrix equality as follows:

$$\mathbf{A}\Upsilon = \Gamma z + \Lambda \tag{17}$$

where

$$\mathbf{A} = \begin{bmatrix} \sigma_{11} - \sigma_{13} & \sigma_{21} - \sigma_{23} \\ \sigma_{12} - \sigma_{13} & \sigma_{22} - \sigma_{23} \end{bmatrix},\ \Upsilon = \begin{bmatrix} x \\ y \end{bmatrix},\ \Gamma = \begin{bmatrix} \sigma_{33} - \sigma_{31} \\ \sigma_{33} - \sigma_{32} \end{bmatrix},\ \Lambda = \begin{bmatrix} \lambda_1 - \lambda_3 \\ \lambda_2 - \lambda_3 \end{bmatrix}$$

If the matrix $\mathbf{A}$ is invertible, the solution for (17) can be obtained by a matrix inversion and can be given as follows:

$$\Upsilon = \mathbf{A}^{-1}\Gamma z + \mathbf{A}^{-1}\Lambda \tag{18}$$

For the proof that $\mathbf{A}$ is invertible, the reader is referred to the Appendix. The solution of (10) can be derived by defining the vectors:

$$\mathbf{m} = \begin{bmatrix} 1 & 0 \end{bmatrix} \tag{19}$$

$$\mathbf{n} = \begin{bmatrix} 0 & 1 \end{bmatrix} \tag{20}$$

Making use of (18), one can obtain the expression for x and y in terms of z as follows:

$$x = \mathbf{m}\mathbf{A}^{-1}\Gamma z + \mathbf{m}\mathbf{A}^{-1}\Lambda \tag{21}$$

$$y = \mathbf{n}\mathbf{A}^{-1}\Gamma z + \mathbf{n}\mathbf{A}^{-1}\Lambda \tag{22}$$

Without loss of generality, one can rewrite (21) and (22) as follows:

$$x = g_1 z + e_1 \tag{23}$$

$$y = g_2 z + e_2 \tag{24}$$

https://doi.org/10.1017/S0263574719000092 Published online by Cambridge University Press

where $\{g_1, g_2, e_1, e_2\} \in \mathbb{R}^{1\times 1}$. Having the expression of x and y, one can now make the substitution back to (10) for any one of the $i = \{1, 2, 3\}$. Picking $i = 1$, the following quadratic equation can be obtained:

$$(g_1 z + e_1)^2 + (g_2 z + e_2)^2 + z^2 + \sigma_{11}\,(g_1 z + e_1) + \sigma_{21}\,(g_2 z + e_2) + \sigma_{31} z = \lambda_1 \tag{25}$$

The terms in (25) can be grouped, and the following simplified expression for z can be obtained:

$$\eta z^2 + \kappa z + \delta = 0 \tag{26}$$

where

$$\eta = g_1^2 + g_2^2 + 1 \tag{27}$$

$$\kappa = 2e_1 g_1 + 2e_2 g_2 + \sigma_{11} g_1 + \sigma_{21} g_2 + \sigma_{31} \tag{28}$$

$$\delta = e_1^2 + e_2^2 + \sigma_{11} e_1 + \sigma_{21} e_2 - \lambda_1 \tag{29}$$

The two roots of (26) can directly be written as follows:

$$z_{1,2} = \frac{-\kappa \pm \sqrt{\kappa^2 - 4\eta\delta}}{2\eta} \tag{30}$$

Here, the roots represent the upper and lower configurations of the delta robot discussed before. From a geometrical point of view, these roots represent the z-axis coordinates for the intersection points of the end effector with the surfaces of the spheres centered at points P_{ci} with radii of l_i as illustrated in Fig. 5. In order to find the correct value for z, the root that corresponds to the upper configuration can be taken as follows:

$$z = \frac{-\kappa + \sqrt{\kappa^2 - 4\eta\delta}}{2\eta} \tag{31}$$

Once z is obtained, one can further proceed to calculate x and y using (23) and (24), respectively, which concludes the forward kinematics calculations. In order to summarize the forward kinematics an algorithmic recipe is given below:

Algorithm 1 Summary of forward kinematics

Given the system configuration parameters α_i and θ_i, the lengths l_i, r_e and r_b, and the actuator displacements d_i for $i = \{1, 2, 3\}$:

- Calculate $\sigma_{1i}, \sigma_{2i}, \sigma_{3i}, \lambda_i$
- Form matrices $\mathbf{A}$, Γ, Λ
- Calculate g_1, g_2, e_1, e_2
- Calculate η, κ, δ
- $z = \frac{-\kappa + \sqrt{\kappa^2 - 4\eta\delta}}{2\eta}$
- $y = g_2 z + e_2$
- $x = g_1 z + e_1$

4. Position-level Inverse Kinematics

Similar to the forward kinematics, Eq. (9) constitutes the basis for the derivation of the inverse kinematics. However, here the positions x, y and z are known while the actuator displacements d_i's are unknown. Rearranging (9) for the unknown terms, one can obtain the following expression:

$$d_i^2 + \mu_{1i} d_i + \mu_{2i} = 0 \tag{32}$$

where the terms μ_{1i} and μ_{2i} have the following contents:

$$\mu_{1i} = 2c\alpha_i\,(r_e - r_b + c\theta_i x + s\theta_i y) - 2s\alpha_i z \tag{33}$$

$$\mu_{2i} = -l_i^2 + x^2 + y^2 + z^2 + (r_e - r_b)\,(r_e - r_b + 2c\theta_i x + 2s\theta_i y) \tag{34}$$

https://doi.org/10.1017/S0263574719000092 Published online by Cambridge University Press

The expression given in (32) contains three quadratic equations; each of which includes a single unknown d_i for $i = \{1, 2, 3\}$, respectively. The solutions can be obtained using discriminant analysis as follows:

$$\Delta_i = \mu_{1i}^2 - 4\mu_{2i} \tag{35}$$

Similar to the forward kinematics, one will have two roots using the Δ_i's above:

$$d_{i_{1,2}} = \frac{-\mu_{1i} \pm \sqrt{\Delta_i}}{2} \tag{36}$$

Under the condition that $\|.\|$ represents L_2 norm, (6) geometrically reflects spheres for each one of $i = \{1, 2, 3\}$. However, unlike the forward kinematics case, now the solution comes from the intersection of the spheres centered at points P_{ei} with the corresponding actuation axis. Hence, the feasible solution among the two solutions of (32) would be the one that has lower magnitude, which can be given as follows:

$$d_i = \frac{-\mu_{1i} - \sqrt{\Delta_i}}{2} \tag{37}$$

For the sake of completeness, the algorithmic procedure of the inverse kinematics calculations is given below:

Algorithm 2 Summary of inverse kinematics

Given the system configuration parameters α_i and θ_i, the lengths l_i, r_e and r_b for $i = \{1, 2, 3\}$ and the end effector coordinates $\{x, y, z\}$;

- Calculate μ_{1i}, μ_{2i}
- Calculate Δ_i
- $d_i = \frac{-\mu_{1i} - \sqrt{\Delta_i}}{2}$

5. Velocity-level Kinematics

In order to obtain the velocity-level kinematics of the system being analyzed, one can again refer to the constraining equation given in (9). Differentiating that equation gives:

$$f_{di}(t)\dot{d}_i(t) = f_{xi}(t)\dot{x}(t) + f_{yi}(t)\dot{y}(t) + f_{zi}(t)\dot{z}(t) \tag{38}$$

where the functions $f_{xi}(t)$, $f_{yi}(t)$, $f_{zi}(t)$ and $f_{di}(t)$ for $i = \{1, 2, 3\}$ have the following content:

$$f_{xi}(t) = c\theta_i\ (r_b - r_e - c\alpha_i d_i(t)) - x(t) \tag{39}$$

$$f_{yi}(t) = s\theta_i\ (r_b - r_e - c\alpha_i d_i(t)) - y(t) \tag{40}$$

$$f_{zi}(t) = s\alpha_i d_i(t) - z(t) \tag{41}$$

$$f_{di}(t) = c\alpha_i\ (r_e - r_b + c\theta_i x(t) + s\theta_i y(t)) - s\alpha_i z(t) + d_i(t) \tag{42}$$

The objective of velocity-level kinematics is to come up with the mapping between the joint (i.e., configuration) space velocities $\dot{\mathbf{q}}(t) = \left[\dot{d}_1(t), \dot{d}_2(t), \dot{d}_3(t)\right]^T$ and the task (i.e., operational) space velocities $\dot{\mathbf{x}}(t) = \left[\dot{x}(t), \dot{y}(t), \dot{z}(t)\right]^T$. To formulate that mapping, one can diagonalize the terms $f_{di}(t)$ of (42) and write down the following identity:

$$\mathbf{J_q}\dot{\mathbf{q}}(t) = \mathbf{J_x}\dot{\mathbf{x}}(t) \tag{43}$$

where the contents of matrices $\mathbf{J_q}$ and $\mathbf{J_x}$ are given as follows:

$$\mathbf{J_q} = \begin{bmatrix} f_{d1}(t) & 0 & 0 \\ 0 & f_{d2}(t) & 0 \\ 0 & 0 & f_{d3}(t) \end{bmatrix} \tag{44}$$

https://doi.org/10.1017/S0263574719000092 Published online by Cambridge University Press

$$\mathbf{J_x} = \begin{bmatrix} f_{x1}(t) & f_{y1}(t) & f_{z1}(t) \\ f_{x2}(t) & f_{y2}(t) & f_{z2}(t) \\ f_{x3}(t) & f_{y3}(t) & f_{z3}(t) \end{bmatrix} \tag{45}$$

Making use of (43), one can formulate the kinematic Jacobian $\mathbf{J}$ of the system as follows:

$$\mathbf{J} = \mathbf{J_x}^{-1}\mathbf{J_q} \tag{46}$$

The Jacobian matrix derived in (46) plays an important role for the practical applications since both the force and velocity mappings between the configuration and operational spaces are carried out using it. The existence of Jacobian matrix is dependent on the non-singular structure of matrix $\mathbf{J}$. This matrix is singular if any of the matrices $\mathbf{J_x}$ or $\mathbf{J_q}$ is rank deficient. The analysis of the singular configurations of the system under consideration is carried out in the next section, where a similar generalized parametric study is conducted.

6. Generalized Singularity Analysis

As mentioned in the previous section, singular configurations of the linear delta robot can be obtained from the content of the matrices $\mathbf{J_x}$ and $\mathbf{J_q}$. In order to obtain all of the possible singularities of the generalized system, these two matrices are investigated independently in the following subsections.

6.1. Analysis of matrix $\boldsymbol{J_q}$

The singularity analysis of the matrix $\mathbf{J_q}$ is relatively straight forward since it has a diagonal structure: This matrix is singular if any of the diagonal elements is equal to zero. Thus, the singular configurations exist if $f_{di}(t) = 0$ for $i \in \{1, 2, 3\}$. However, the content of $f_{di}(t)$ given in Eq. (42) include variables x, y and z which makes the analysis difficult. In order to modify (42) and get $f_{di}(t)$ without the end effector coordinates, one can benefit from Eq. (8) as follows:

$$x = v_{i,x} - (r_e - r_b + d_i c\alpha_i)\, c\theta_i \tag{47}$$

$$y = v_{i,y} - (r_e - r_b + d_i c\alpha_i)\, s\theta_i \tag{48}$$

$$z = v_{i,z} + d_i s\alpha_i \tag{49}$$

where $v_{i,x}$, $v_{i,y}$ and $v_{i,z}$ stand for the principle components of the vector $\mathbf{v}_i$ that extends from bottom point (P_{ci}) to the top point (P_{ei}) of the link l_i with respect to the base coordinate frame Ψ_B (i.e., $\|\mathbf{v}_i\| = l_i$ and $\mathbf{v}_i = \left[v_{i,x}, v_{i,y}, v_{i,z}\right]^T$). Now, with these new definitions, one can substitute (47)–(49) back to (42). Removing the time component (t) for simpler analysis and carrying out the necessary trigonometric cancellations (i.e., $c^2\theta_i + s^2\theta_i = 1$ and $c^2\alpha_i + s^2\alpha_i = 1$) one can get the following identity:

$$f_{di} = v_{i,x} c\alpha_i c\theta_i + v_{i,y} c\alpha_i s\theta_i - v_{i,z} s\alpha_i \tag{50}$$

Having a detailed look on (50), one can observe that f_{di} is basically the dot product of vector $\mathbf{v}_i$ with another vector $\mathbf{u}_i = [c\alpha_i c\theta_i, c\alpha_i s\theta_i, -s\alpha_i]^T$ (i.e., $f_{di} = \langle \mathbf{v}_i, \mathbf{u}_i \rangle = \mathbf{v}_i^T \mathbf{u}_i$ for $i = \{1, 2, 3\}$). Further, inspecting the vector $\mathbf{u}_i$, one can realize that $\mathbf{u}_i = R_{z,\theta_i} R_{y,\alpha_i} \mathbf{w}$, where $\mathbf{w} = [1, 0, 0]^T$ represent the unit vector along x-axis of the base frame Ψ_b. In other words, vector $\mathbf{u}_i$ is obtained by two consecutive rotations of vector $\mathbf{w}$ around fixed y- and z-axes by angles of α_i and θ_i, respectively. Geometrically, this means that the vector $\mathbf{u}_i$ is parallel to the actuation axis i. In order to reinforce the discussion, vectors $\mathbf{u}_i$, $\mathbf{v}_i$ and $\mathbf{w}$ are clearly indicated in Fig. 6. Since this dot product is basically the projection of vector $\mathbf{v}_i$ over the vector $\mathbf{u}_i$, f_{di} will become zero (and hance a singular configuration will occur) if the vector $\mathbf{v}_i$ is orthogonal to the corresponding actuation axis d_i.

6.2. Analysis of matrix $\boldsymbol{J_x}$

The singularity analysis of the matrix $\mathbf{J_x}$ seems more complicated since it contains many off-diagonal elements. However, the definitions given in Eqs. (47)–(49) also help us to simplify the content of this

https://doi.org/10.1017/S0263574719000092 Published online by Cambridge University Press

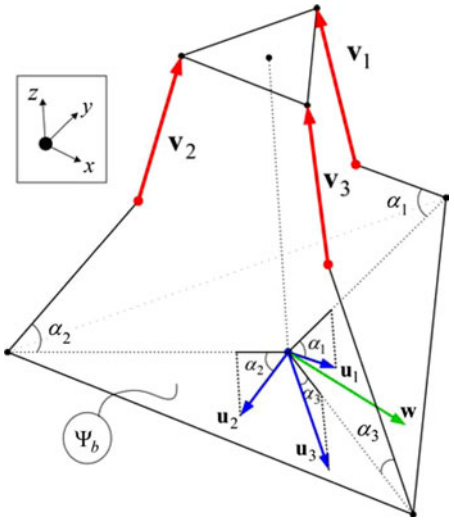


Fig. 6. Depiction of the vectors $\mathbf{u}_i$, $\mathbf{v}_i$ and $\mathbf{w}$ used in the singularity analysis.

matrix. Substituting (47), (48) and (49), respectively, back to (39), (40) and (41) and evaluating the matrix $\mathbf{J_x}$, one can get the following expression:

$$\mathbf{J_x} = \begin{bmatrix} -v_{1,x} & -v_{2,x} & -v_{3,x} \\ -v_{1,y} & -v_{2,y} & -v_{3,y} \\ -v_{1,z} & -v_{2,z} & -v_{3,z} \end{bmatrix} = \begin{bmatrix} -\mathbf{v}_1 & -\mathbf{v}_2 & -\mathbf{v}_3 \end{bmatrix} \tag{51}$$

The result obtained in (51) tells us that the columns of the matrix $\mathbf{J_x}$ are actually negatives of the vectors $\mathbf{v}_i$ for $i = \{1, 2, 3\}$. In other words, this matrix is formed by the vectors pointing along the links l_i. From a linear algebraic perspective, it is easy to deduce that the singular structure of $\mathbf{J_x}$ exists whenever the vectors $\mathbf{v}_i$ cannot span the 3D-space. This can happen when the arms l_i are either coplanar or collinear. Hence, the structures where the links l_i become all vertical or all horizontal are among the examples of the singular configurations of the linear delta robot. Referring back to (51), a final type of singularity comes into picture when one of the arms of l_i becomes parallel to the plane spanned by the other two arms.

6.3. Summary of singular configurations

Based on the analysis presented in the preceding subsections, a prismatically actuated delta robot would fall into singularity:

- if any one of the arms l_i become perpendicular to the corresponding actuation axis d_i
- if all of the arms l_i become perpendicular to the base plane
- if all of the arms l_i become parallel to the base plane
- if one of the arms l_i becomes parallel to the plane spanned by the remaining two arms

7. Experiments

In order to validate the equations derived in this paper, the forward and the inverse kinematics algorithms are tested in real experiments. The experimental setups are explained in the following subsections along with the results obtained from the experiments.

7.1. Experimental platforms

In order to test the proposed generalized kinematic formulation, two prismatically actuated delta robot configurations, namely the horizontal and the Keops configurations, are selected as the experimental platforms. In both configurations, the angles between the projections of actuation axes on the base plane are taken to be equal (i.e., $2\pi/3$ radians) to each other, forming an equilateral triangle for the base and end effector. By doing so, the angles of the system under consideration become $\theta_1 = 90°$, $\theta_2 = 210°$ and $\theta_3 = 330°$. In the horizontal structure, all of the attack angles α_i have 0 radian value whereas in the Keops configuration, the attack angles are selected to be $\pi/6$

https://doi.org/10.1017/S0263574719000092 Published online by Cambridge University Press

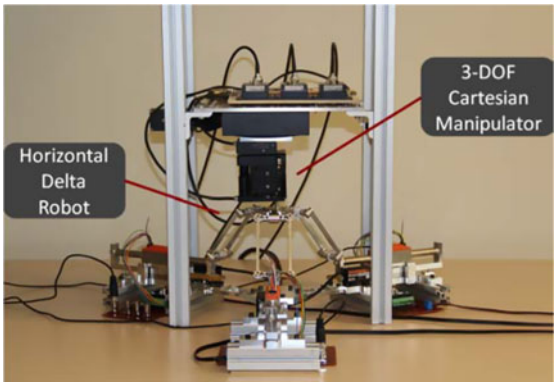


Fig. 7. The experimental platform depiction for the horizontal delta configuration.

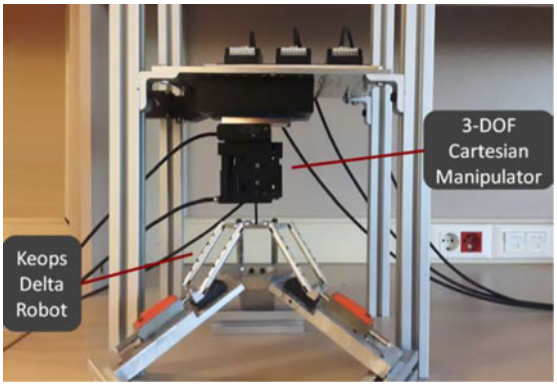


Fig. 8. The experimental platform depiction for the Keops delta configuration.

radians. Each delta platform consists of three direct drive linear motors of Faulhaber LM series and aluminum links and joints. The actuators of horizontal delta system have integrated encoders from Renishaw with a resolution of $0.5\mu m$ while the position measurements of the actuators of Keops delta system are handled via using the hall-effect sensors integrated to the motors.

For the purpose of verification, another 3-DOF manipulator is designed and attached to the end effectors of the delta robots. This manipulator is a Cartesian manipulator consisted of linear actuators driven by rotary motors and ball-screw mechanisms. The aim of using a Cartesian robot is to have the ability of both actuation and precise measurement in three orthogonal axes of the end effectors of delta robots. Although such a validation could also be made by using the CAD models, high-precision and continuous sampling of the motion from CAD files of the robots would require very long simulation durations and quite a big computational power. Furthermore, the experimental validation also helps on the evaluation of the computational load of the kinematics and Jacobian calculation algorithms for the real-time applications, which would not be possible should the validation be made on a CAD model.

The selected Cartesian robot contains motors from PI-M111 series all of which have internal encoders that can sense as small as 50 nm of linear motion due to high gain in the ball screw. The end effectors of the Cartesian manipulator and the delta robots (both for Keops and for horizontal configurations) are connected via a solid metal connector which precisely synchronizes the motions of the end effectors. Depictions of the experimental platforms are given in Figs. 7 and 8 for the experimental validation of the kinematics of horizontal and Keops configurations, respectively.

7.2. Experiment results

Throughout the experiments, the Cartesian manipulator is controlled under step references of 5 mm, and the real-time responses are measured. For the verification of forward kinematics, the position response of the Cartesian manipulator is compared with the calculated forward kinematics response of delta robots using the joint displacements. The results are shown in Figs. 9 and 12 for the horizontal

https://doi.org/10.1017/S0263574719000092 Published online by Cambridge University Press

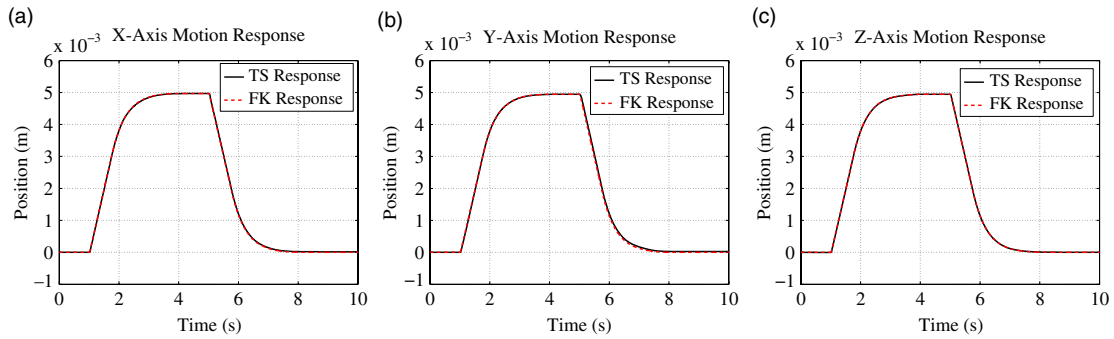


Fig. 9. Validation of forward kinematics response for horizontal configuration.

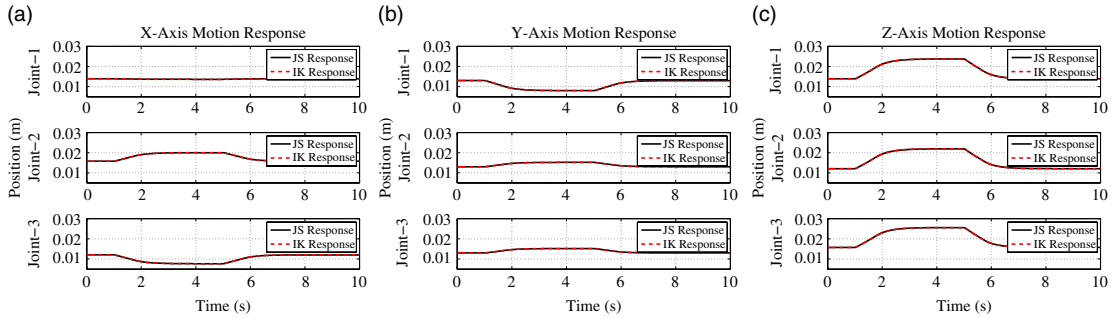


Fig. 10. Validation of inverse kinematics response for horizontal configuration.

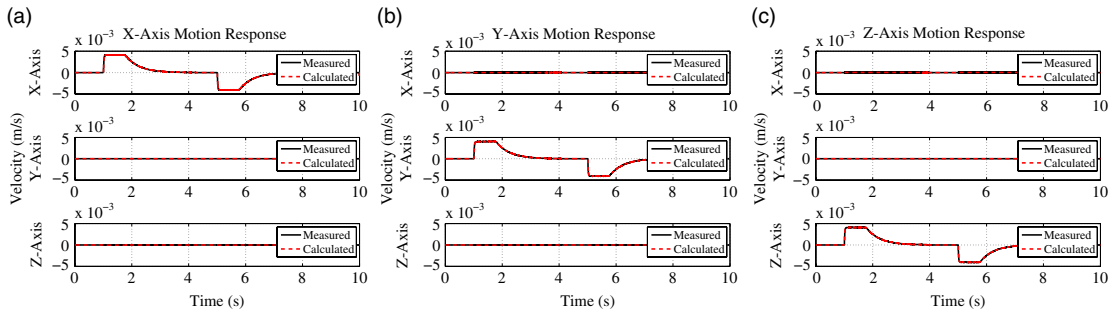


Fig. 11. Validation of kinematic Jacobian for horizontal configuration.

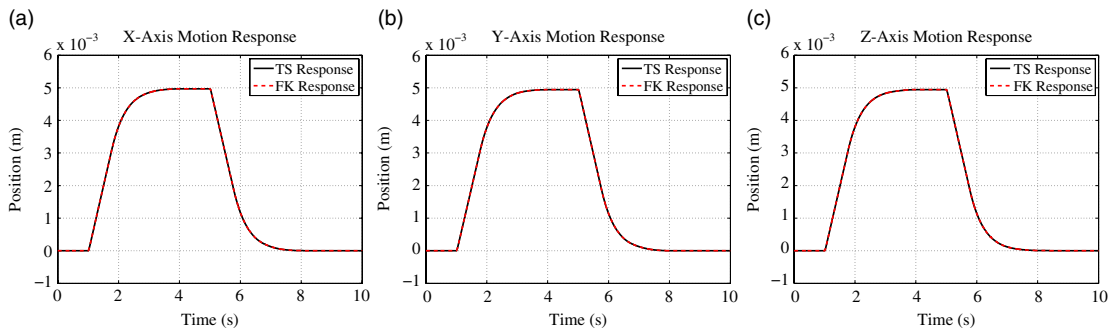


Fig. 12. Validation of forward kinematics response for Keops configuration.

and Keops delta configurations, respectively. In these figures, the abbreviations *FK* and *TS* stand for forward kinematics and task space, respectively.

For the verification of the inverse kinematics, the motion of the Cartesian manipulator is used as the input, and the responses are compared with the measurements obtained from the delta robot joints. The results of inverse kinematics validation are illustrated for horizontal and Keops delta robots in

https://doi.org/10.1017/S0263574719000092 Published online by Cambridge University Press

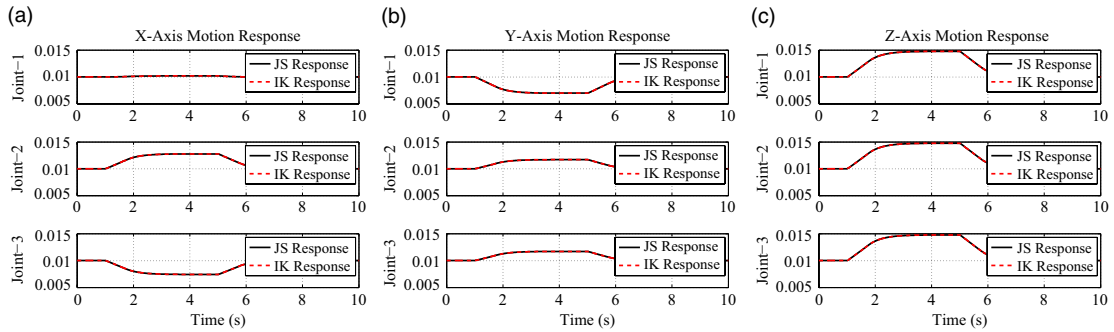


Fig. 13. Validation of inverse kinematics response for Keops configuration.

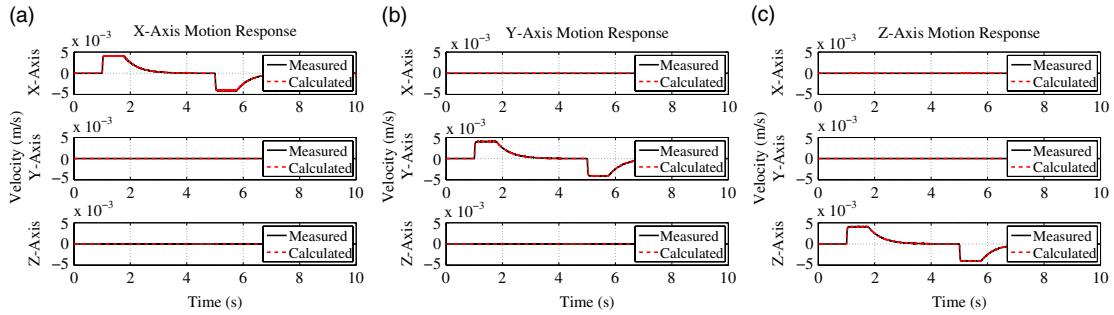


Fig. 14. Validation of kinematic Jacobian for Keops configuration.

Figs. 10 and 13, respectively. The abbreviations *IK* and *JS* represent the inverse kinematics and joint space, respectively.

The verification of the kinematic Jacobian is made by following a slightly more complicated path. The position measurements of the delta robot joints are differentiated to get the joint velocities. These differentiations are made using the Backward Euler method and are low pass filtered with a cut-off frequency of 317 rad/s (i.e., 2 KHz) in order to remove the noise over the responses. Since the selected references have a low-frequency behavior, applying a filter at 2 KHz does not influence the original dynamics of the responses. These velocities are then multiplied by the corresponding kinematic Jacobians to calculate the end effector velocities. The calculated velocities are compared with the velocities obtained by differentiating the position measurement of Cartesian manipulator using the same method, and the results are shown in Figs. 11 and 14 for horizontal and Keops systems, respectively. In these figures, the data with the label "Measured" represent the differentiated end effector position while the data with the label "Calculated" stand for the velocities obtained from joints using Jacobian. As can be seen from the figures, the formulation made throughout the paper shows one to one correspondence with the actual measurements.

8. Benchmark Study for Optimal Cubic Workspace

Benefiting from the flexible approach brought by the parametric derivation given above, the maximum cubic workspace of the symmetric and the semi-symmetric linear delta robot configurations are calculated. These configurations are ones for which the intersection points of actuator axes with the base plane create isosceles triangles as shown in Fig. 2(A)–(C). In order to simplify the optimization process, a new intermediate angle "ρ" is introduced and the angles between the projections of the actuator axes over the base plane are redefined as follows:

$$\theta_1 = 90^\circ \qquad \theta_2 = (180 + \rho)^\circ \qquad \theta_3 = (360 - \rho)^\circ \tag{52}$$

where ρ is one of the two parameters used in the optimization process. The second optimization parameter is selected as the angle α_i, where all three angles for $i = 1, 2, 3$ have the same value to keep rest of the system symmetric. In other words, the optimized structure has:

$$\alpha_1 = \alpha^\circ \qquad \alpha_2 = \alpha^\circ \qquad \alpha_3 = \alpha^\circ \tag{53}$$

https://doi.org/10.1017/S0263574719000092 Published online by Cambridge University Press

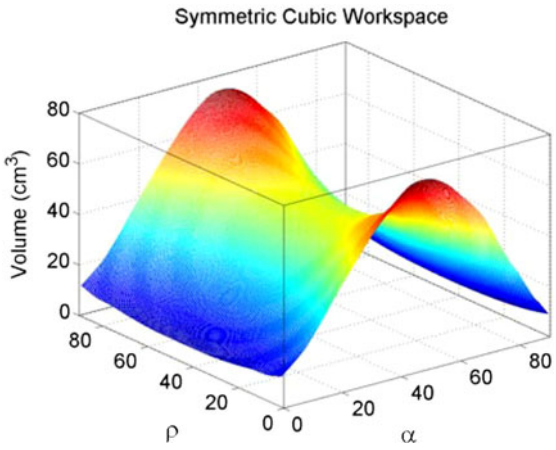


Fig. 15. Maximum symmetric (i.e., cubic) workspace volume.

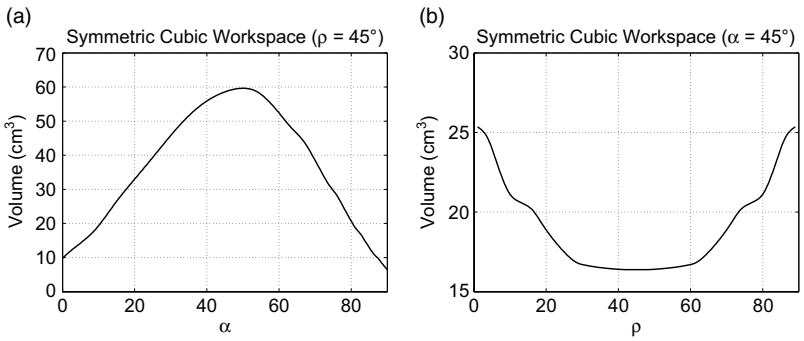


Fig. 16. Maximum symmetric workspace variation for angles α and ρ.

The other variables of the linear delta robot being optimized are selected as $r_e = 0.044$ m, $r_b = 0.121$ m, $l_i = 0.091$ m and $d_i \in [0, 0.06]$ m for $i = 1, 2, 3$.

For the calculation of the maximum symmetric workspace, these two angles of interest are swept in the ranges $0 \leq \alpha^\circ \leq 90^\circ$ and $1 \leq \rho^\circ \leq 89^\circ$ by increments of one degrees, respectively. During these sweeps, for each $[\alpha, \rho]$ couple, the volume of the maximum cubic workspace are calculated. In order to find the cube that fits inside the reachable workspace created by the selected $[\alpha, \rho]$ couple with the maximum volume, first a small cube with a very short edge length is selected and positioned to the center of the workspace. Then with very small increments, the edge length of the cube is increased. For each new cube, an algorithm using inverse kinematics checked whether 8 corner points and 6 additional points positioned at the centers of each face of that cube is inside the reachable workspace of the system. The volume of the cube is increased until any of these 14 points exceeds the reachable workspace and this way the cube with the maximum volume is attained for the selected $[\alpha, \rho]$ pair.

The results obtained from these simulations are plotted in a 3D graph in Fig. 15. In order to provide further insight of the results, cross-sections from the graph given in Fig. 15 are taken at angles $\rho = 45^\circ$ and $\alpha = 45^\circ$. The plots of these cross-sections are given in Fig. 16.

Analyzing the responses shown in Figs. 15 and 16, one can observe that the maximum cubic workspace is attained for the attack angle $\alpha_i = 50^\circ$ for $i = 1, 2, 3$ for the entire range of $0 < \rho^\circ < 90^\circ$. Considering the effect of the parameter ρ, $\rho = 1^\circ$, and $\rho = 89^\circ$ give almost the same workspace volumes, respectively.

In order to provide further insight on the optimization process, the cubes with the maximum volume fitting inside the workspace of particular configurations are plotted within the total workspace of the corresponding systems. As the maximum cube volumes are always obtained for the angle $\alpha = 50^\circ$, these plots are taken particularly for that angle value. On the other hand, the angle ρ is selected where the maximum and minimum values of cubic volumes are attained (i.e., $\rho = 89^\circ$, $\rho = 45^\circ$ and $\rho = 1^\circ$), and the results are shown in 3D plots in Fig. 17. For better illustration, projections of total and maximum cubic workspaces on $X - Y$, $X - Z$ and $Y - Z$ planes are taken and are shown in Figs. 18, 19 and 20, respectively.

https://doi.org/10.1017/S0263574719000092 Published online by Cambridge University Press

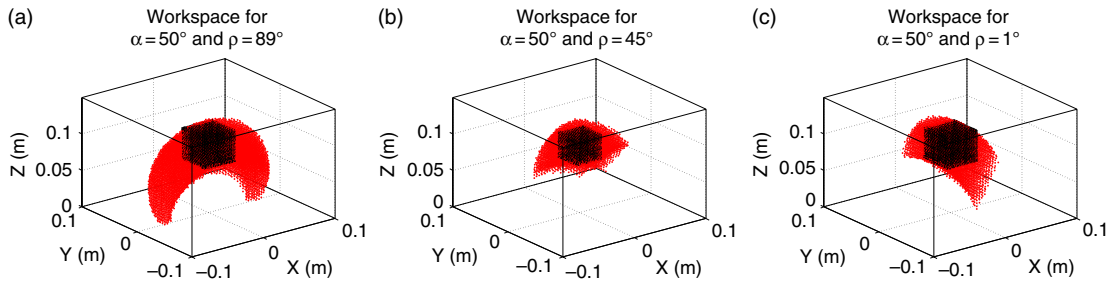


Fig. 17. Workspaces with variation of angle ρ (red dots: total workspace, black dots: maximum cubic workspace fitting in total workspace.)

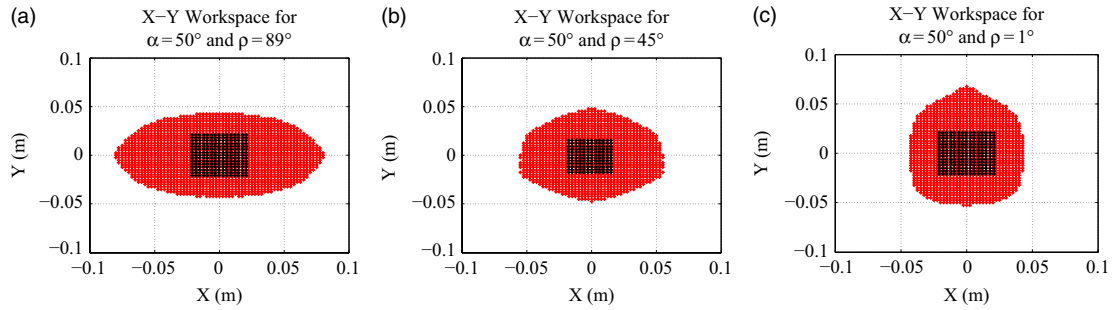


Fig. 18. $X-Y$ workspaces with variation of angle ρ (red area: total workspace, black area: maximum cubic workspace fitting in total workspace.)

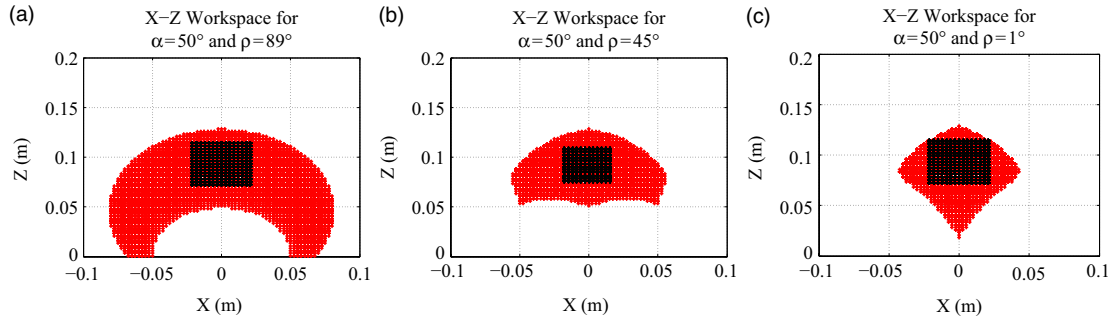


Fig. 19. $X-Z$ workspaces with variation of angle ρ (red area: total workspace, black area: Maximum cubic workspace fitting in total workspace.)

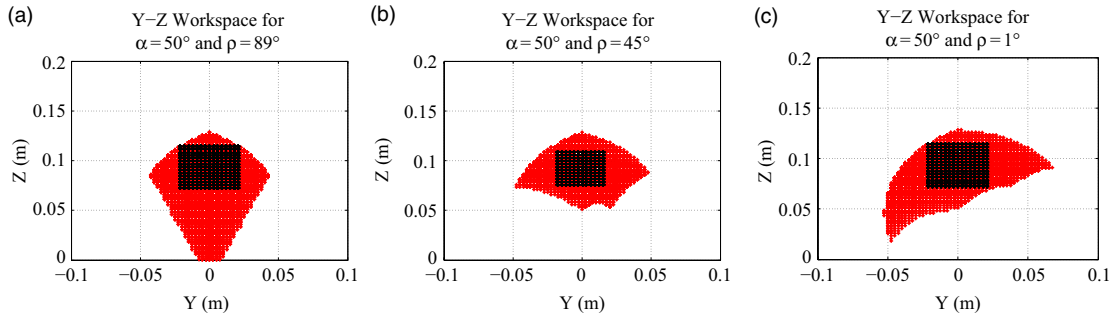


Fig. 20. $Y-Z$ workspaces with variation of angle ρ (red area: total workspace, black area: maximum cubic workspace fitting in total workspace.)

8.1. Effect of the lengths on the maximum symmetric workspace

The optimal workspace calculated in the previous section is obtained assuming that the lengths l_i, r_e and r_b are kept constant. This subsection is reserved for the analysis of the effects of these three

https://doi.org/10.1017/S0263574719000092 Published online by Cambridge University Press

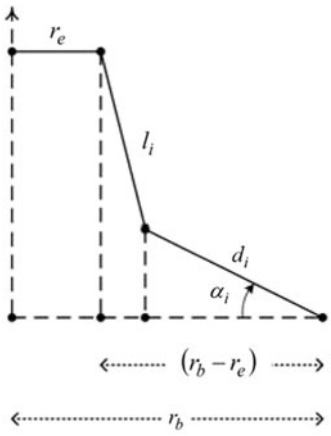


Fig. 21. Cross-section of the system geometry along an actuation axis.

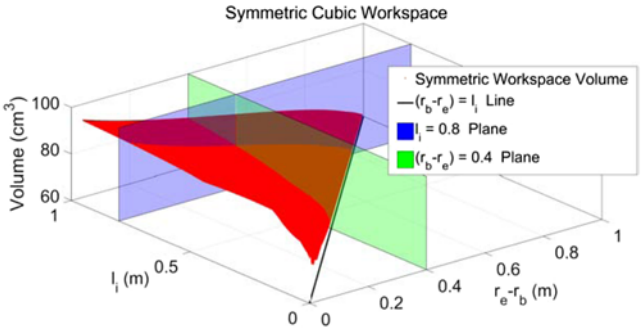


Fig. 22. Maximum symmetric (i.e., cubic) workspace volume.

parameters over the maximum cubic workspace of the delta robot. The rest of the discussion is based on the depiction shown in Fig. 21.

Referring to Fig. 21 and to the analysis made in Section 6, one can deduce that the singular configurations would be avoided if

- $d_{\max} c\alpha_i < (r_b - r_e) \Rightarrow$ hence, l_i is never vertical
- $(r_b - r_e) < l_i \Rightarrow$ hence, l_i is never horizontal

where $0 \leq d_i \leq d_{\max}$. In other words, the condition

$$d_{\max} c\alpha_i < (r_b - r_e) < l_i \tag{54}$$

provides a singularity-free workspace for any value of the angles α_i and θ_i within their allowable ranges defined in Section 2. In order to evaluate the effect of these lengths on the maximum symmetric workspace, a series of simulations are made where the lengths $(r_b - r_e)$ and l_i are varied without violating the condition given in (54). In favor of clearly observing the effects, these two lengths are extended to extreme values the and the corresponding maximum symmetric workspace volumes are calculated using the approach discussed in the previous section. The results of these simulations are shown in Fig. 22. For the sake of better illustration, this 3D plot is cut by two vertical planes placed on $l_i = 0.8$ and $(r_b - r_e) = 0.4$, and the resulting 2D plots are shown in Fig. 23(A) and 23(B), respectively.

The results given in Figs. 22 and 23 and Eq. (54) indicate several interesting features for the linear delta robots. The first one is that the difference between r_b and r_e affects the workspace rather than the independent absolute values of these two lengths. The second salient observation is that the volume of the maximum cubic workspace increases by increasing l_i, decreasing $(r_b - r_e)$ or doing both of them. So, keeping in mind the constraint set by Eq. (54), one can conclude that the maximum non-singular cubic workspace is attained by minimizing $(r_b - r_e)$ and maximizing l_i. However, even

https://doi.org/10.1017/S0263574719000092 Published online by Cambridge University Press

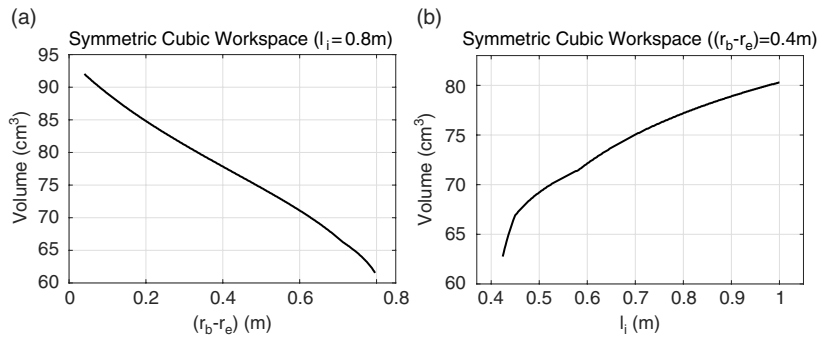


Fig. 23. Maximum symmetric workspace variation for lengths l_i and $(r_b - r_e)$.

though $(r_b - r_e)$ has a lower limit, there is no upper limit for the length l_i. In that sense, the designers, willing to obtain the maximum cubic workspace would be constrained by the physical properties (i.e., motor driving capabilities and inertias of the arms) of the system being considered.

9. Conclusion and Future Work

9.1. Conclusion

In this study, a generalized framework is proposed for the kinematic analysis of the family of parallel delta robots with prismatic actuation. The presented analysis covers the derivation of the position- and velocity-level kinematics and the formulation of the kinematic Jacobian assuming variable parameters for all of the configuration angles and link lengths. Benefiting from the exact solutions obtained from a geometry based approach, the proposed method enables the direct (i.e., non-iterative) computation of kinematics for linear delta robots that have different and potentially asymmetric configurations as also illustrated in Figs. 2–4. Such a generalized formulation, also being applicable for the asymmetric configurations, brings the ability to design completely novel structures targeting specific objectives like increased positioning accuracy in desired axes. Further, a similar parametric analysis is made for the identification of all of the possible singular configurations for the system under consideration. Hence, the proposed framework brings the ability to avoid singular configurations right from the design phase of such novel mechanisms. Another advantage of the proposed formulation is to provide the designer with the necessary mathematical background for multiobjective and possibly multicriteria optimization studies, opening the path through optimally designed structures targeting specific goals. This advantage is also emphasized with a benchmark optimization study illustrating the relationship between the maximum cubic workspace volume and two of the system parameters for the symmetric and semi-symmetric configurations of linear delta robots. The proposed framework is experimentally validated on two variants of delta robot family. The results obtained from the benchmark study and the real-time experiments highlight the flexible and wide-range application possibility of the presented generalized formulation.

9.2. Future work

Originating from the fully parametric analysis given in this study, the authors are now investigating the possibility of carrying out multidimensional constrained optimization to come up with new configurations to satisfy certain goals. The objective is to achieve the highest possible motion resolution and largest workspace along a single axis of motion via adjusting the angles α_i and θ_i and the lengths l_i, r_e and r_b. Such a structure will be working close to the boundary of redundancy exhibiting negligible motion along the axis orthogonal to the optimized motion axis. On the other hand, the optimized structure will be useful in applications that require high precision, rapid operation and large range of motion.

Acknowledgments

The authors would gratefully acknowledge Tubitak Projects 110M425 and 114M578 for the partial financial supports provided for this research.

https://doi.org/10.1017/S0263574719000092 Published online by Cambridge University Press

References

1. V. Pozhbelko, E. Kuts, "Structural synthesis and analysis of multiple-jointed mechanical systems and industrial application for robot manipulator," *Proc. Eng.* **206** 1774–1779 (2017).
2. Z. Zhakypov, T. Uzunovic, A. O. Nergiz, E. A. Baran, E. Golubovic, A. Sabanovic, "Desktop Microfactory for High Precision Assembly and Machining," *Industrial Electronics (ISIE), 2014 IEEE 23rd International Symposium on IEEE*, Istanbul, Turkey (2014) pp. 1192–1197.
3. M. Dogar, R. A. Knepper, A. Spielberg, C. Choi, H. I. Christensen, D. Rus, "Towards Coordinated Precision Assembly with Robot Teams," *Experimental Robotics,* vol. 109 (Springer, Cham, 2016) pp. 655–669.
4. A. Pourkand, N. Zamani, D. Grow, "Mechanical model of orthopaedic drilling for augmented-haptics-based training," *Comput. Biol. Med.* **89**, 256–263 (2017).
5. L. Feng, P. Di, F. Arai, "High-precision motion of magnetic microrobot with ultrasonic levitation for 3-d rotation of single oocyte," *Int. J. Robot. Res.* **35** (12), 1445–1458 (2016).
6. Y. Li, Y. Ma, S. Liu, Z. Luo, J. Mei, T. Huang, D. Chetwynd, "Integrated design of a 4-dof high-speed pick-and-place parallel robot," *CIRP Ann. Manuf. Technol.* **63** (1), 185–188 (2014).
7. A. Cammarata, "Optimized design of a large-workspace 2-dof parallel robot for solar tracking systems," *Mech. Mach. Theor.* **83** 175–186 (2015).
8. M. A. Hosseini, H. Daniali, "Cartesian workspace optimization of tricept parallel manipulator with machining application," *Robotica* **33** (9), 1948–1957 (2015).
9. R. Kelaiaia, A. Zaatri, L. Chikh, et al., "Some investigations into the optimal dimensional synthesis of parallel robots," *Int. J. Adv. Manuf. Technol.* **83** (9–12), 1525–1538 (2016).
10. J. Wu, X. Chen, L. Wang, "Design and dynamics of a novel solar tracker with parallel mechanism," *IEEE/ASME Trans. Mechatron.* **21** (1), 88–97 (2016).
11. Y. Zhao, K. Qiu, S. Wang, Z. Zhang, "Inverse kinematics and rigid-body dynamics for a three rotational degrees of freedom parallel manipulator," *Robot. Comput.-Integr. Manuf.* **31** 40–50 (2015).
12. S. Seriani, M. Seriani, P. Gallina, "Workspace optimization for a planar cable suspended direct-driven robot," *Robot. Comput.-Integr. Manuf.* **34** 1–7 (2015).
13. H. Shi, X. Duan, H.-J. Su, "Optimization of the Workspace of a Mems Hexapod Nanopositioner using an Adaptive Genetic Algorithm," *Robotics and Automation (ICRA), 2014 IEEE International Conference on IEEE*, Hong Kong, China (2014) pp. 4043–4048.
14. S. S. Ganesh, A. K. Rao, "Optimal workspace volume of two configurations of 3-dof pkm," *Indian J. Sci. Technol.* **10** (46).
15. A. Kosinska, M. Galicki, K. Kedzior, "Designing and optimization of parameters of delta-4 parallel manipulator for a given workspace," *J. Robot. Syst.* **20** (9), 539–548 (2003).
16. P. K. Jamwal, S. Hussain, S. Q. Xie, "Three-stage design analysis and multicriteria optimization of a parallel ankle rehabilitation robot using genetic algorithm," *IEEE Trans. Automation Sci. Eng.* **12** (4), 1433–1446 (2015).
17. H. Shin, J.-H. Moon, "Design of a double triangular parallel mechanism for precision positioning and large force generation," *IEEE/ASME Trans. Mechatron.* **19** (3), 862–871 (2014).
18. R. Kelaiaia, O. Company, A. Zaatri, "Multiobjective optimization of a linear delta parallel robot," *Mech. Mach. Theor.* **50** 159–178 (2012).
19. D. Zhang, Z. Gao, "Performance analysis and optimization of a five-degrees-of freedom compliant hybrid parallel micromanipulator," *Robot. Comput.-Integr. Manuf.* **34** 20–29 (2015).
20. S. Yan, S. Ong, A. Nee, "Stiffness analysis of parallelogram-type parallel manipulators using a strain energy method," *Robot. Comput.-Integr. Manuf.* **37** 13–22 (2016).
21. K. Miller, "Maximization of workspace volume of 3-dof spatial parallel manipulators," *J. Mech. Design* **124** (2), 347–350 (2002).
22. F. Xie, X.-J. Liu, X. Chen, J. Wang, "Optimum Kinematic Design of a 3-dof Parallel Kinematic Manipulator with Actuation Redundancy," *Intelligent Robotics and Applications. ICIRA 2011*, Lecture Notes in Computer Science, vol. 7101 (Springer, Berlin-Heidelberg, 2011) pp. 250–259.
23. M. A. Mousavi, M. T. Masouleh, A. Karimi, "On the maximal singularity-free ellipse of planar 3-rpr parallel mechanisms via convex optimization," *Robot. Comput.-Integr. Manuf.* **30** (2), 218–227 (2014).
24. J. Borras, F. Thomas, C. Torras, "New geometric approaches to the analysis and design of stewartgough platforms," *IEEE/ASME Trans. Mechatron.* **19** (2), 445–455 (2014).
25. M. Lopez, E. Castillo, G. Garca, A. Bashir, "Delta robot: inverse, direct, and intermediate- jacobians, Proceedings of the Institution of Mechanical Engineers, Part C:." *J. Mech. Eng. Sci.* **220** (1), 103–109 (2006).
26. K. Hsu, M. Karkoub, M.-C. Tsai, M. Her, "Modelling and index analysis of a delta-type mechanism," *Proc. Inst. Mech. Eng. Part K: J. Multi-body Dyn.* **218** (3), 121–132 (2004).
27. N. Plitea, A. Szilaghyi, D. Pisla, "Kinematic analysis of a new 5-dof modular parallel robot for brachytherapy," *Robot. Comput.-Integr. Manuf.* **31** 70–80 (2015).
28. H. Saafi, M. A. Laribi, S. Zeghloul, "Forward kinematic model improvement of a spherical parallel manipulator using an extra sensor," *Mech. Mach. Theor.* **91** 102–119 (2015).
29. H. S. Bidokhti, J. Enferadi, "Direct Kinematics Solution of 3-rrr Robot by using Two Different Artificial Neural Networks," *Robotics and Mechatronics (ICROM), 2015 3rd RSI International Conference on IEEE*, Tehran, Iran (2015) pp. 606–611.
30. X. Yang, H. Wu, Y. Li, B. Chen, "A dual quaternion solution to the forward kinematics of a class of six-dof parallel robots with full or reductant actuation," *Mech. Mach. Theor.* **107** 27–36 (2017).

https://doi.org/10.1017/S0263574719000092 Published online by Cambridge University Press

31. Y. Jin, Z. Bi, H. Liu, C. Higgins, M. Price, W. Chen, T. Huang, "Kinematic analysis and dimensional synthesis of exechon parallel kinematic machine for large volume machining," *J. Mech. Robot.* **7** (4), 041004 (2015).
32. F. Xie, X.-J. Liu, Z. You, J. Wang, "Type synthesis of 2t1r-type parallel kinematic mechanisms and the application in manufacturing," *Robot. Comput.-Integr. Manuf.* **30** (1), 1–10 (2014).
33. J. E. Correa, J. Toombs, N. Toombs, P. M. Ferreira, "Laminated micro-machine: Design and fabrication of a flexure-based delta robot," *J. Manuf. Process.* **24** 370–375 (2016).
34. A. Martini, M. Troncossi, M. Carricato, A. Rivola, "Static balancing of a parallel kinematics machine with linear-delta architecture: Theory, design and numerical investigation," *Mech. Mach. Theor.* **90** 128–141 (2015).
35. G. C. Anzalone, B. Wijnen, J. M. Pearce, "Multi-material additive and subtractive prosumer digital fabrication with a free and open-source convertible delta reprap 3-d printer," *Rapid Prototyping J.* **21** (5), 506–519 (2015).
36. E. A. Baran, T. E. Kurt, A. Sabanovic, "Lightweight Design and Encoderless Control of a Miniature Direct Drive Linear Delta Robot," *Electrical and Electronics Engineering (ELECO), 2013 8th International Conference on IEEE*, Bursa, Turkey (2013) pp. 502–506.
37. H. Azulay, M. Mahmoodi, R. Zhao, J. K. Mills, B. Benhabib, "Comparative analysis of a new 3 pprs parallel kinematic mechanism," *Robot. Comput.-Integr. Manuf.* **30** (4), 369–378 (2014).
38. W.-H. Yuan, M.-S. Tsai, "A novel approach for forward dynamic analysis of 3-prs parallel manipulator with consideration of friction effect," *Robot. Comput.-Integr. Manuf.* **30** (3), 315–325 (2014).
39. Q. Zeng, K. F. Ehmann, J. Cao, "Tri-pyramid robot: Design and kinematic analysis of a 3-dof translational parallel manipulator," *Robot. Comput.-Integr. Manuf.* **30** (6), 648–657 (2014).
40. J. Pile, N. Simaan, "Modeling, design, and evaluation of a parallel robot for cochlear implant surgery," *IEEE/ASME Trans. Mechatron.* **19** (6), 1746–1755 (2014).
41. Y. Li, Q. Xu, "Design and development of a medical parallel robot for cardiopulmonary resuscitation," *IEEE/ASME Trans. Mechatron.* **12** (3), 265–273 (2007).
42. Y. Li, Q. Xu, "Kinematic analysis of a 3-prs parallel manipulator," *Robot. Comput.-Integr. Manuf.* **23** (4), 395–408 (2007).

Appendix

Proof of invertibility of matrix ***A***

The matrix **A** of (17) consists of the terms given in Eqs. (11)–(13). The invertibility of this matrix can be verified by checking its determinant. However, direct substitution of σ_{ij} will generate a highly complicated expression for the determinant. Instead, one can first simplify the content of matrix **A** and then make the analysis further. For this purpose, one can define the following intermediate expression:

$$\zeta_i = d_i \cos(\alpha_i) + r_e - r_b \tag{55}$$

With that expression in hand, substituting the content of abbreviated σ_{ij} terms from (11) to (13), one can write the content of matrix **A** as follows:

$$\mathbf{A} = 2\begin{bmatrix} c\theta_1\zeta_1 - c\theta_3\zeta_3 & s\theta_1\zeta_1 - s\theta_3\zeta_3 \\ c\theta_2\zeta_2 - c\theta_3\zeta_3 & s\theta_2\zeta_2 - s\theta_3\zeta_3 \end{bmatrix} \tag{56}$$

where $c\theta_i$ and $s\theta_i$ stand for the cosine and sine terms, respectively. Now, with that structure of matrix **A**, one can calculate its determinant as follows:

$$\begin{aligned} det(\mathbf{A}) = &-\zeta_1\zeta_2 c\theta_2 s\theta_1 + \zeta_1\zeta_2 c\theta_1 s\theta_2 - \zeta_1\zeta_3 c\theta_1 s\theta_3 \\ &+\zeta_1\zeta_3 c\theta_3 s\theta_1 - \zeta_2\zeta_3 c\theta_3 s\theta_2 + \zeta_2\zeta_3 c\theta_2 s\theta_3 \end{aligned} \tag{57}$$

which can be further simplified using trigonometric identities as follows:

$$det(\mathbf{A}) = \zeta_1\zeta_3 \sin(\theta_1 - \theta_3) - \zeta_1\zeta_2 \sin(\theta_1 - \theta_2) - \zeta_2\zeta_3 \sin(\theta_2 - \theta_3) \tag{58}$$

Looking at the system geometry given in Fig. 1, one can observe that the terms $\zeta_i < 0$ and hence $\zeta_i\zeta_j > 0$ for all $i, j \in \{1, 2, 3\}$. Having kept this in mind, the analysis of (58) can proceed with the analysis of sine terms. Referring to the angle definitions given in Fig. 1, one can write down the following information related to the signs of the sine terms:

https://doi.org/10.1017/S0263574719000092 Published online by Cambridge University Press

$$\begin{aligned} -2\pi < (\theta_1 - \theta_3) < -\pi &\Rightarrow \sin(\theta_1 - \theta_3) > 0 \\ -\pi < (\theta_1 - \theta_2) < 0 &\Rightarrow \sin(\theta_1 - \theta_2) < 0 \\ -\pi < (\theta_2 - \theta_3) < 0 &\Rightarrow \sin(\theta_2 - \theta_3) < 0 \end{aligned} \tag{59}$$

With these information related to the signs of the terms in (58), one can conclude that for all feasible values of angles θ_i and all values $\alpha_i \in [0, \pi/2]$ with $i \in 1, 2, 3$, the following can be obtained:

$$det(\mathbf{A}) > 0 \tag{60}$$

■

https://doi.org/10.1017/S0263574719000092 Published online by Cambridge University Press